nature communications

Article

https://doi.org/10.1038/s41467-025-59645-x

Fast product release requires active-site water dynamics in carbonic anhydrase

Received: 17 August 2024

Accepted: 30 April 2025

Jin Kyun Kim[1,12], Seon Woo Lim[1], Hannah Jeong[1], Cheol Lee[1], Seoyoon Kim[2], Dong Woo Son[3,4], Rajeev Kumar[5,6], Jacob T. Andring[7], Carrie Lomelino[7], Jennifer L. Wierman[8], Aina E. Cohen[9], Tae Joo Shin[10], Cheol-Min Ghim[1], Robert McKenna[7], Byung Hoon Jo[3,4,11], Duyoung Min[2], Jeong-Mo Choi[5,6] & Chae Un Kim[1]

Water plays an essential role in enzyme structure, stability, and the substantial rate enhancement of enzyme catalysis. However, direct observations linking enzyme catalysis and active-site water dynamics pose a significant challenge due to experimental difficulties. By integrating an ultraviolet (UV) photolysis technique with temperature-controlled X-ray crystallography, we track the catalytic pathway of carbonic anhydrase II (CAII) at 1.2 Å resolution. This approach enables us to construct molecular movies of CAII catalysis, encompassing substrate (CO_2) binding, conversion from substrate to product (bicarbonate), and product release. In the catalytic pathway, we identify an unexpected configuration in product binding and correlate it with sub-nanosecond rearrangement of active-site water. Based on these experimental observations, we propose a comprehensive mechanism of CAII and describe the detailed structure and dynamics of active-site water in CAII. Our findings suggest that CAII has evolved to utilize the structure and fast dynamics of the active-site waters for its diffusion-limited catalytic efficiency.

Enzymatic reactions are complex multistep chemical processes that proceed at astonishingly enhanced rates of up to 10^{19} fold, when compared to their counterpart processes in aqueous solution alone[1,2]. Various mechanisms for the speed of enzymatic reactions have been proposed, including the concepts of transition state stabilization, ground-state destabilization, entropy effects, spatiotemporal effects, near-attack conformation, electrostatic preorganization, solvent pre-organization, and quantum mechanical tunneling[3–13]. More recently, these theories of enzyme catalysis have been further complicated by the dynamic motions of enzymes[14–23].

When considering the dynamic properties of enzymes, it has been noted that they are intricately linked to the conformational changes and the motion of water molecules within and surrounding the enzyme active site[24–26]. Indeed, water should be treated as an integral and active component of the active site; water molecules are essential participants in the overall stability, structure, and dynamics of enzymes.

---

[1]Department of Physics, Ulsan National Institute of Science and Technology (UNIST), Ulsan 44919, Republic of Korea. [2]Department of Chemistry, Ulsan National Institute of Science and Technology (UNIST), Ulsan 44919, Republic of Korea. [3]Division of Applied Life Science (BK21 Four), Gyeongsang National University, Jinju 52828, Republic of Korea. [4]Anti-Aging Bio Cell Factory Regional Leading Research Center (ABC-RLRC), Gyeongsang National University, Jinju 52828, Republic of Korea. [5]Department of Chemistry, Pusan National University, Busan 46241, Republic of Korea. [6]Chemistry Institute for Functional Materials, Pusan National University, Busan 46241, Republic of Korea. [7]Department of Biochemistry and Molecular Biology, University of Florida, Gainesville, FL 32610, USA. [8]Cornell High Energy Synchrotron Source, Cornell University, Ithaca, New York 14853, USA. [9]Stanford Synchrotron Radiation Lightsource, SLAC National Accelerator Laboratory, Menlo Park, California 94025, USA. [10]Graduate School of Semiconductor Materials and Devices Engineering, Ulsan National Institute of Science and Technology (UNIST), Ulsan 44919, Republic of Korea. [11]Research Institute of Life Science, Gyeongsang National University, Jinju 52828, Republic of Korea. [12]Present address: Frontier of Extreme Physics, Korea Research Institute of Standards and Science, Daejeon 34113, Republic of Korea. e-mail: cukim@unist.ac.kr

Additionally, water molecules play an essential role in enzyme catalysis, actively participating in molecular recognition by mediating interactions between binding partners and contributing to either enthalpic or entropic stabilization[27,28]. In this regard, understanding the detailed interplay between water and enzymes at the molecular level is a topic of significant interest and a central goal in protein science and enzymology. However, very little is known about how water structure and dynamics are directly linked to enzymatic mechanisms, such as substrate binding, transition state stabilization, and product release. Molecular details linking the fast water dynamics (sub-nanosecond range) to the enzyme catalysis is particularly scarce, as determining detailed catalytic pathways at both ~1 Å spatial resolution and sub-ns time resolution is challenging using experimental methods. To date, no enzymatic reaction has been characterized in enough detail to reveal a complete mechanism of water structure and dynamics for enzyme catalysis. In this study, we have experimentally tracked down the structure and dynamics of active-site water in carbonic anhydrase during its catalytic reaction.

Carbonic anhydrase (CA) is mainly a zinc-containing metalloenzyme, ubiquitous across all animals and photosynthesizing organisms as well as in some non-photosynthetic bacteria, and is one of the most catalytically efficient enzymes known[29–34] (Supplementary Table 1). The enzyme catalyzes the reversible hydration of carbon dioxide (CO_2), playing a crucial role in respiration. In the human body, it facilitates CO_2 transport through blood-dissolved bicarbonate (HCO_3^-) and maintains intracellular pH homeostasis by regulating CO_2/HCO_3^- equilibrium.

Among the 15 different human CA isozymes, carbonic anhydrase II (CAII) has a rapid CO_2 hydration turnover rate of ~$10^6\,s^{-1}$ under physiological conditions and has thus been extensively studied as a model system for enzymes with fast kinetics[35–39]. The active site of CAII is situated within a central cavity, ~15 Å deep from the surface. It comprises an entrance conduit with both hydrophobic and hydrophilic sides, along with a catalytic core centered around a zinc ion (Fig. 1a)[40–44]. This zinc ion is tetrahedrally coordinated by three histidine residues (His94, His96, and His119) and a water/hydroxide. Within this active site, hydrophobic residues (Val121, Val143, Leu198, and Trp209) form a substrate binding pocket conducive to CO_2 binding. In this pocket, the CO_2 molecule and the zinc-bound hydroxide are held in close proximity and proper orientation, facilitating the conversion to product[44]. The product, bicarbonate, is generated through a nucleophilic attack by the zinc-bound hydroxide, which is then exchanged with incoming water molecules. Finally, the zinc-bound water molecule is converted to a hydroxide ion, while a proton is transferred out via a water network (W1, W2, and W3a-b; Fig. 1b). This proton transfer water network is stabilized by hydrophilic residues (Tyr7, Asn62, Asn67, Thr199, and Thr200) and is connected to His64, the proton shuttling residue[45].

Previously, the catalytic mechanism of CAII has been studied by cryo-trapping the CO_2-CAII complex under pressures of up to 20

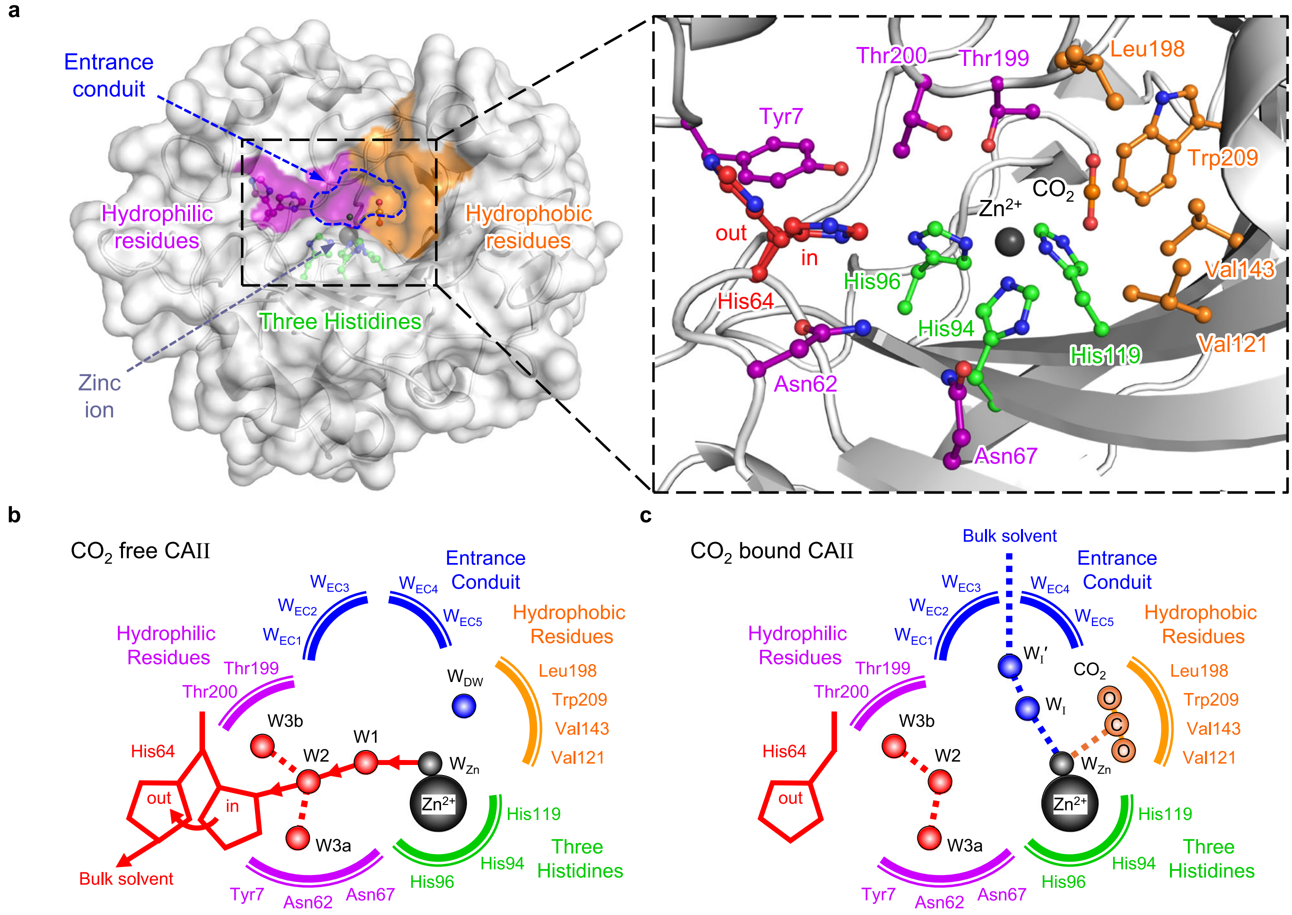

Fig. 1 | Overall structure and active-site water network of CAII. a The overall shape of CAII. The active site contains hydrophobic residues (orange) that facilitate substrate (CO_2) binding and hydrophilic residues (purple) that support proton transfer through an ordered water network. The blue dotted line indicates the entrance conduit connecting the exterior to the active site. **b** The active-site water network of CAII without CO_2 binding. Five water molecules at the entrance conduit ($W_{EC1\text{-}5}$), deep water (W_{DW}), Zn^{2+}-bound water (W_{Zn}), and the proton transfer water network (W1, W2, and W3a-b) are well-ordered. His64, the proton-shuttling residue, adopts dynamic 'in' and 'out' positions. **c)** The active-site water network of CAII with CO_2 binding. Upon CO_2 binding, W_{DW} is displaced by CO_2, leading to the emergence of two intermediate water molecules (W_I and $W_I{'}$).

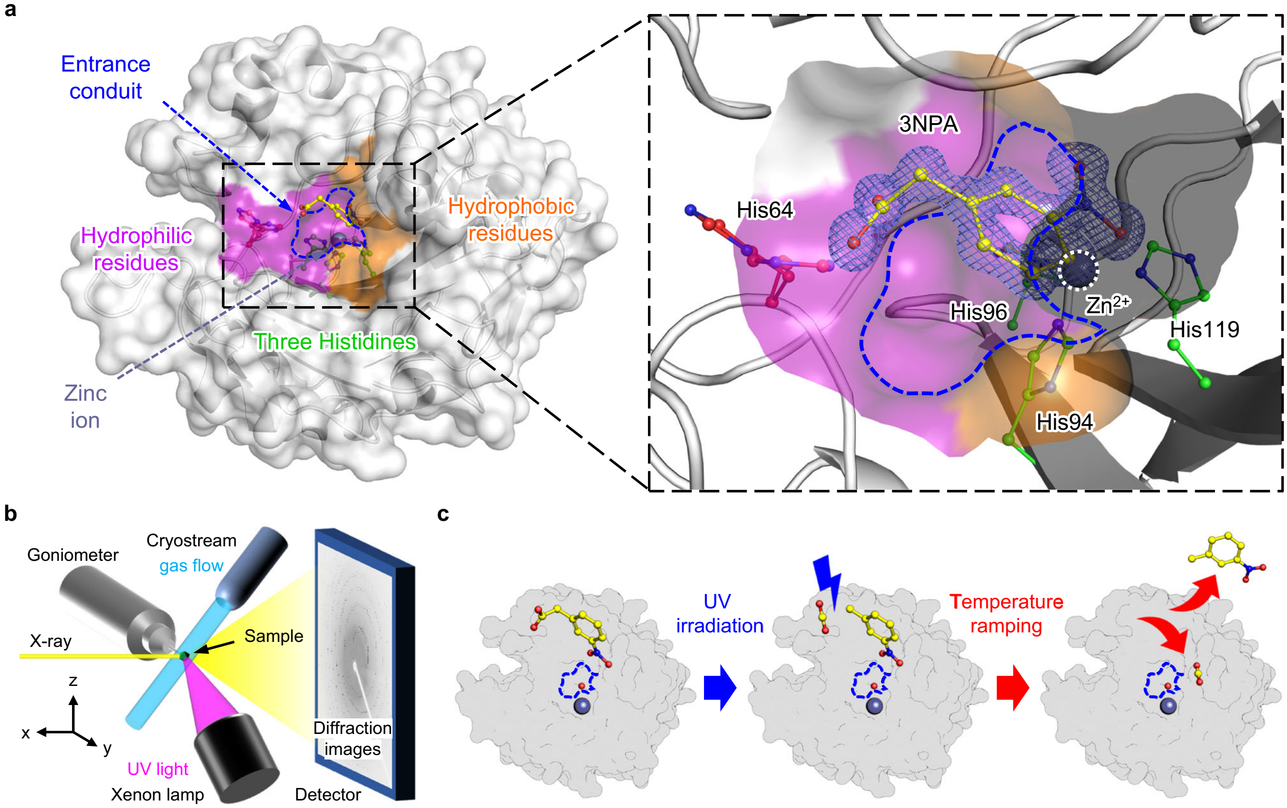

Fig. 2 | Overall shape of 3NPA-CAII complex and the experimental procedure. **a** The overall structure of the 3NPA-CAII complex. The colored regions represent the hydrophobic region (orange) and the hydrophilic region (purple), while the blue dotted line marks the entrance conduit. 3NPA binds at the entrance, interacting with active-site residues and the Zn^{2+} ion. The electron density map ($2F_o - F_c$) of 3NPA is from the 3NPA-CAII-noUV-90K (1.2 Å resolution with a cutoff level of 2.0σ). **b** Experimental scheme for UV photolysis and temperature-controlled crystallography. The CAII crystal sample is irradiated with focused UV light from a Xenon lamp and kept at cryogenic temperature by the N_2 cold gas flow from the cryostream. Diffraction images are collected at specific temperatures regulated by the cryostream. **c** Conceptual illustration of the experimental procedure. The CAII molecule is simplified in gray, while the Zn^{2+} ion, 3NPA, CO_2, and 3NT molecules are enlarged for clarity.

atm[43,44,46,47]. These CAII structures presented the initial substrate binding steps of the catalytic pathway. The crystallographic intermediates revealed a highly organized water structure within the active site of CAII, which underwent reorganization upon substrate binding (Fig. 1b, c and Supplementary Fig. 1).

In this study, we employed a UV photolysis technique followed by temperature-controlled X-ray crystallography to capture an extended series of intermediate structures, enabling the construction of a molecular movie depicting the CAII catalytic pathway. During the UV photolysis step, we used 3-nitrophenyl acetic acid (3NPA) as a photocaged molecule due to its small molecular size (181 g/mol) and high dissociation quantum yield in the UV range (0.63 at 367 nm)[48,49]. Our findings indicate that 3NPA binds within the CAII active site cavity (Fig. 2a). The structure of the 3NPA-CAII complex reveals that 3NPA is stabilized by interactions with active-site residues and the Zn^{2+} ion (Supplementary Fig. 2). Upon UV-light irradiation at 90 K (Fig. 2b), 3NPA undergoes photolysis, converting to 3-nitrotoluene (3NT) and releasing CO_2. Due to limited diffusion at cryogenic temperatures, both molecules remain stationary within the active site. As the temperature increases, 3NT exits the active site, while CO_2 diffuses toward the Zn^{2+} ion, initiating the CAII-catalyzed hydration reaction (Fig. 2c). This approach allowed us to observe substrate binding, conversion from substrate to product (bicarbonate), and product release. Our findings propose a detailed mechanism for CAII, demonstrating that its catalytic process relies on the intricate structure and sub-nanosecond dynamics of active-site waters. This proposed mechanism could provide valuable insights into the catalytic processes of carbonic anhydrases in other organisms, including the recently discovered metal-free CA[50,51].

Results

Structural and catalytic impact of 3NPA and 3NT on CAII

Before tracking the catalytic pathways of CAII, we first investigated the structural and catalytic impact of 3NPA and 3NT on CAII. Crystallographic studies revealed that 3NPA remains stably bound to CAII across the entire experimental temperature range (90 K to room temperature) when the 3NPA-CAII complex has not been exposed to UV light (Supplementary Fig. 3). Structural comparisons between ligand-unbound CAII and the 3NPA-CAII complex showed that 3NPA binding has a negligible effect on the overall structure of CAII (C_α r.m.s.d. <0.16 Å, Supplementary Fig. 4). When the 3NPA-CAII complex was cryocooled under elevated CO_2 pressure, CO_2 was properly positioned in the active site, while the occupancy of 3NPA was reduced (Supplementary Fig. 5). This result suggests that 3NPA may compete with the substrate for binding in the active site. However, kinetic measurements indicate that 3NPA has minimal impact on the CO_2 hydration reaction of CAII, retaining ~98% of k_{cat}/K_M and ~86% of k_{cat} compared to native CAII (Supplementary Fig. 6).

Upon UV irradiation, the electron density of 3NPA split into two, consistent with the formation of 3NT and CO_2 at cryogenic temperatures (Supplementary Fig. 7). However, soaking CAII crystals in a 3NT solution revealed that 3NT does not stably bind to the CAII active site (Supplementary Fig. 5). Structural comparisons between native CAII and 3NT-soaked CAII showed that 3NT had a negligible effect on the overall structure of CAII (C_α r.m.s.d. <0.18 Å, Supplementary Fig. 4) and did not noticeably alter the active-site water structure (Supplementary Fig. 5). When the 3NT-soaked CAII was cryocooled under elevated CO_2 pressure, CO_2 was positioned correctly, and active-site water molecules were rearranged in the same manner as in native CAII (Supplementary Fig. 5). This result indicates that 3NT has minimal impact on the structure and catalytic intermediates of CAII. Indeed, kinetic measurements reveal that 3NT has an insignificant effect on the CO_2 hydration reaction of CAII, retaining ~83% of k_{cat}/K_M and ~94% of k_{cat} compared to native CAII (Supplementary Fig. 6).

Tracking catalytic pathways of CAII

To capture the catalytic pathways of CAII, the 3NPA-CAII crystal was carefully irradiated with UV light ($\lambda = 200–400$ nm) at 90 K, ensuring that the bound 3NPA converted to 3NT and CO_2 (Methods and Supplementary Figs. 8 and 9). The crystal was then sequentially warmed to 200 K. A series of complete X-ray crystallographic data sets were collected at 90 K (before and after UV irradiation), 120 K, 140 K, 160 K, 180 K, and 200 K from a single 3NPA-CAII crystal. The refined structures are designated as follows: 3NPA-CAII-noUV-90K, 3NPA-CAII-UV-90K, 3NPA-CAII-UV-120K, 3NPA-CAII-UV-140K, 3NPA-CAII-UV-160K, 3NPA-CAII-UV-180K, and 3NPA-CAII-UV-200K, respectively. As a control, we also collected the X-ray crystallographic data sets from a Zn^{2+}-free 3NPA-apoCAII crystal under the same experimental conditions. These refined structures are designated as 3NPA-apoCAII-noUV-90K, 3NPA-apoCAII-UV-90K, 3NPA-apoCAII-UV-120K, 3NPA-apoCAII-UV-140K, 3NPA-apoCAII-UV-160K, 3NPA-apoCAII-UV-180K, and 3NPA-apoCAII-UV-200K, respectively.

The active site structures of CAII after the 3NPA photolysis are presented in Fig. 3. Right after UV irradiation, 3NPA dissociates, and a limited amount of CO_2 molecules and an active-site water molecule (W_{DW}) diffuse into the active site. As temperature increases from 90 K,

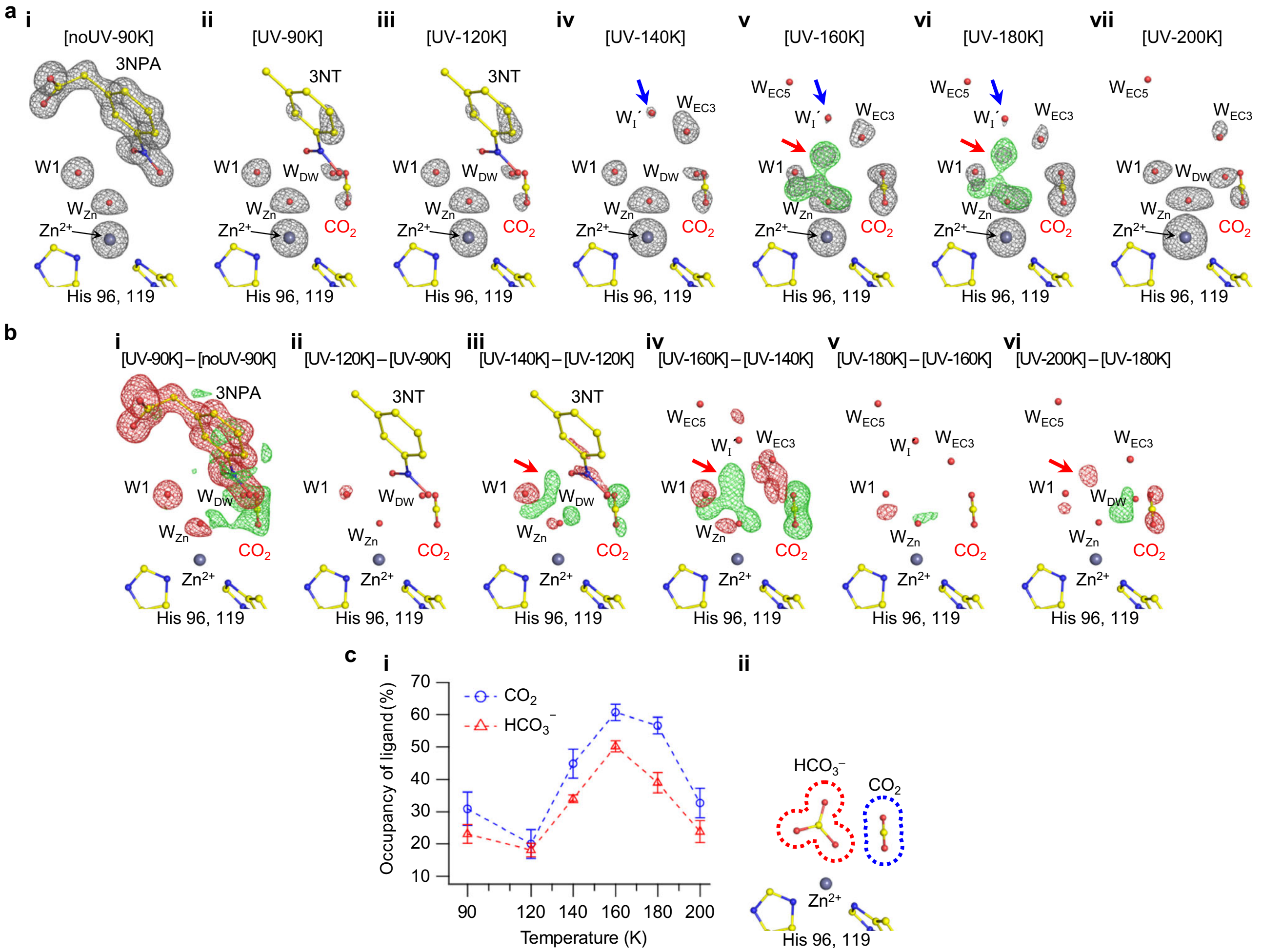

Fig. 3 | Structures of 3NPA-CAII complex before and after UV irradiation. **a** Before UV irradiation at 90 K (noUV-90K), 3NPA is clearly visible. After UV irradiation at the same temperature (UV-90K), 3NPA disappears, and 3NT, partially occupied W_{DW}, and CO_2 emerge. As the temperature increases to 160 K, W_{DW} is further replaced by CO_2. At 160-180 K, the difference map (green) reveals an excess feature (red arrow) that cannot be fitted with either CO_2 or active-site water molecules. The intermediate water $W_I´$ also becomes visible along with this excess feature (blue arrow). At 200 K, both CO_2 and the excess feature diffuse away and are eventually replaced by water molecules (W_{DW}, W1, and W_{Zn}). The electron density map ($2F_o - F_c$, gray) is contoured at a cutoff level of 1.7σ. The difference maps ($F_o - F_c$, green) are contoured at a cutoff level of 6.0σ. **b** The differences in electron density between the 3NPA-CAII temperature series show that CO_2 and the excess feature (red arrow) emerge at 140 K and grow up to 160 K. The excess feature is planar and exhibits three-fold symmetry. The difference electron density maps between structures are expressed as ([B] – [A]); $F_{o,B} - F_{o,A}$, with green/red indicating positive/negative values, contoured at a cutoff level of ±5.0σ, except for ([UV-90K] – [noUV-90K]) and ([UV-200K] – [UV-180K]) which are at ±6.0σ and ±4.0σ, respectively. **c** The partial occupancies of CO_2 and HCO_3^- increase with rising temperature from 120 K to 160 K and then decrease toward 200 K. Each data point represents the occupancy corresponding to the minimum R-factor value from a single dataset, determined through quadratic curve fitting. The associated error bars were estimated by propagating the standard errors of the fitting parameters (Methods). Note that the partial occupancies at 90 K and 120 K are less accurate and exhibit larger standard errors. For reference, the positions of CO_2 and HCO_3^- complexed with CAII are shown on the right side of the graph.

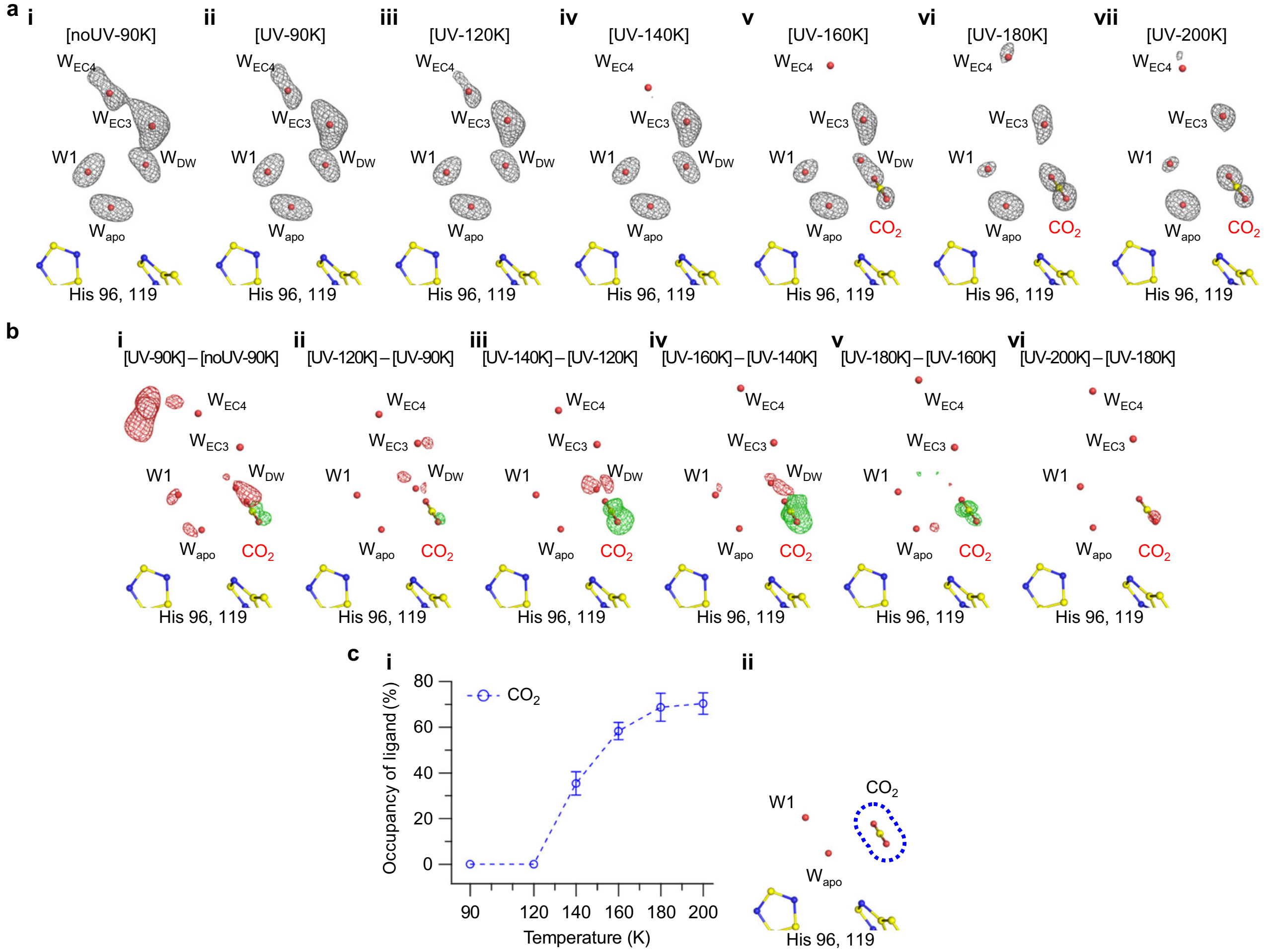

Fig. 4 | Structures of 3NPA-apoCAII complex before and after UV irradiation. **a** Before UV irradiation, the electron density of 3NPA is not observed (noUV-90K). After UV irradiation, the deep-water molecule W_{DW} is substituted with CO_2 as the temperature increases up to 180 K. This CO_2 is likely produced from the 3NPA molecules dissolved in the solvent channels of 3NPA-apoCAII crystal. Note that CO_2 remains at the binding site even at 200 K. The electron density map ($2F_o - F_c$, gray) is contoured at a cutoff level of 1.7σ. **b** Differences in electron density between the 3NPA-apoCAII temperature series show that CO_2 emerges at 140 K, the occupancy increases up to 180 K, and it remains stable at 200 K. Note that no hint of bicarbonate is observed. The difference electron density maps from structure A to B (expressed as ([B] − [A]); $F_{o,B} - F_{o,A}$, green/red for positive/negative values) are contoured at the cutoff level ±5.0σ, except for ([UV-90K]- [noUV-90K]) and ([UV-200K]- [UV-180K]) which are at ±6.0σ and ±4.0σ, respectively. **c** The Partial occupancy of CO_2 increases monotonously with rising temperature from 120 K to 200 K. Each data point represents the occupancy corresponding to the minimum R-factor value from a single dataset, determined through quadratic curve fitting. The associated error bars were estimated by propagating the standard errors of the fitting parameters (Methods) except for 90 K and 120 K. The partial occupancies at 90 K and 120 K are set to 0%, as the quadratic fittings could not reliably determine their minima. As a guide, the position of CO_2 complexed with apoCAII is shown on the right side of the graph.

CO_2 replaces the active-site water molecule (W_{DW}) up to 160-180 K, with the highest occupancy observed at 160 K, then disappears as the temperature further increases to 200 K (Fig. 3a, c and Supplementary Fig. 10). A comparison of 3NPA-CAII-UV-200K with 3NPA-CAII-noUV-90K and ligand-unbound CAII structures indicates that the enzyme resets to its original state as the temperature reaches 200 K (Supplementary Fig. 11). Alongside the CO_2 binding, a build-up of electron density was observed around the Zn^{2+} ion at 160 K and 180 K, eventually being replaced by water molecules at 200 K. To more accurately identify this density cluster at the intermediate temperatures (160–180 K), we calculated the differences in electron density maps between 3NPA-CAII-UV-(temperature) and 3NPA-CAII-UV-(one step higher temperature) (Fig. 3b and Supplementary Fig. 12). The differences in electron density clearly show that this density is planar with three-fold symmetry, and it develops at 140-160 K along with CO_2.

To further investigate this newly observed feature of electron density, the same examination was conducted on 3NPA-apoCAII, which lacks the Zn^{2+} ion (Fig. 4). In contrast to 3NPA-CAII, the electron density of 3NPA molecule was not stabilized in 3NPA-apoCAII (Supplementary Fig. 13). However, after UV irradiation and a subsequent increase in temperature, the CO_2 molecule was captured in the active site of 3NPA-apoCAII (Fig. 4a). Note that CO_2 stabilization at the active site results from hydrophobic interactions with residues lining one side of the active site cavity (Fig. 1c), so that substrate binding does not require the Zn^{2+} ion. However, the new electron density observed in the 3NPA-CAII-UV-160K structure was not detectable and the occupancy of CO_2 continued to increase in the 3NPA-apoCAII temperature series (Fig. 4b, c and Supplementary Figs. 12 and 14). Considering that apoCAII has no enzymatic activity[52,53], we concluded that the newly observed electron density with three-fold symmetry in the 3NPA-CAII temperature series represents the catalytic product, bicarbonate (HCO_3^-), converted from the bound CO_2 molecule during CAII catalysis (Fig. 3c). This interpretation aligns with the CO_2 occupancy profiles in the CAII temperature series (Figs. 3c and 4c). In the 3NPA-apoCAII series, CO_2 occupancy gradually increases as photolysis-induced CO_2 continues to accumulate in the active site. In contrast, in the 3NPA-CAII series, CO_2 occupancy initially increases and then decreases as it is converted to bicarbonate. Correspondingly, bicarbonate occupancy increases as it forms from CO_2 but subsequently decreases as it is replaced by water molecules. Overall, the UV photolysis of the 3NPA-CAII complex followed by the temperature-controlled X-ray crystallography, captures the sequential events of substrate binding, conversion from substrate to product (bicarbonate), product release, and the dynamics of water during this process (Supplementary Movies 1–5).

New configuration of product binding

The 3NPA-CAII-UV-160K refined with both CO_2 and bicarbonate is shown in Fig. 5a. The CO_2 configuration matches observations from previous studies[46,47] (Fig. 1a). However, the observed bicarbonate configuration is new, differing from the previously reported bicarbonate configurations induced by X-ray radiation or stabilized by residue mutations and metal substitutions in CAII (Fig. 5b and Supplementary Fig. 15)[44,54–60]. To evaluate the relative stability of the newly observed bicarbonate configuration in CAII, we performed density functional theory (DFT) calculations. These calculations revealed that the observed bicarbonate configuration aligns with the DFT-optimized configuration, which corresponds to a minimum on the potential energy surface (PES) (Fig. 5c and Supplementary Fig. 16). Additionally, the DFT calculations predicted the possible location of the hydrogen atom in bicarbonate based on the lowest computed relative energy within this semi-constrained system (Fig. 5c, Supplementary Fig. 17, and Supplementary Data 1–4). Remarkably, the bicarbonate configuration we observed here differs from the three configurations proposed in earlier CAII catalytic mechanisms (Fig. 5d–g)[29,61,62]. In the observed bicarbonate configuration, the three oxygen atoms overlap with the positions of three active-site water molecules (Fig. 5a, g). One of these water molecules is the water W1, which belongs to the proton transfer water network and is highly stable and conserved in the ligand-free wild-type CAII (Fig. 1b). Therefore, earlier proposals may not have considered this newly found bicarbonate configuration due to potential steric hindrance with W1.

Rearrangement of active-site water for product binding and release

Steric hindrance between W1 and bicarbonate can be avoided by the dynamic motions of W1[43,47]. In the wild-type CAII, the highly conserved W1 fades, and two intermediate waters (W_I and $W_I{}'$) emerge upon CO_2 binding (Fig. 6a, b and Supplementary Fig. 18). Then, the bicarbonate formed via a nucleophilic attack is temporarily stabilized by occupying the positions of the three active-site water molecules (W_{Zn}, W1, and W_I) and is eventually released by water molecules incoming through the intermediate water positions (W_I and $W_I{}'$) (Fig. 6c, d). Thus, the structure and dynamics of active-site water are critical for stabilizing and releasing the product in CAII.

To confirm the role of active-site water in bicarbonate binding and release, site-directed mutagenesis was performed. Specifically, Thr200, which forms hydrogen bonds with W1, W_I, and $W_I{}'$, was substituted by Val200 (Fig. 6e, f). The T200V (Thr200 → Val200) CAII variant retains an almost identical overall structure to wild-type CAII (C_α r.m.s.d. of ~ 0.18 Å), even near the Val200 position (Supplementary Fig. 19). However, in the T200V CAII variant, W1 occupancy was significantly reduced, and neither W_I nor $W_I{}'$ were detectable upon CO_2 binding (Fig. 6e, f). Notably, under elevated CO_2 pressure, CO_2 binding was not observed in the T200V variant. Instead, bicarbonate was stabilized in a deeper active site configuration than in the 3NPA-CAII-UV-160K (Fig. 6f, Supplementary Figs. 19 and 20). These findings underscore the essential role of active-site waters (W1, W_I, and $W_I{}'$) in CAII catalysis. In wild-type CAII, active-site waters (W1, W_I, and W_{Zn}) are preconfigured in the product binding site, and their dynamic motion facilitates product accommodation and release (Fig. 6c, d). However, in the T200V CAII variant, W1 and W_I are destabilized, causing the product to occupy the deeper active-site positions of W_{Zn} and W_{DW} (Fig. 6g, h). Additionally, the loss of water dynamics due to W_I and $W_I{}'$ destabilization disrupts incoming water flow, hindering efficient product release and further stabilizing product binding (Fig. 6g, h). This interpretation aligns with the observed catalytic inefficiency of the T200V CAII. The catalytic parameters, k_{cat}, and k_{cat}/K_M, at physiological pH 7.1-7.2 indicate that the catalytic activity of T200V CAII decreases to ~11% for k_{cat}/K_M and ~6% for k_{cat} compared to the wild-type CAII[63] (Supplementary Table 1).

Discussion

Timescales of active-site water dynamics

The catalytic mechanism of CAII has a proton transfer process as its rate-limiting step, which occurs immediately after bicarbonate release via the active-site water network toward His64, located at the rim of the active site entrance[38]. Given that the turnover number (k_{cat}) of CAII is ~$10^6\ s^{-1}$ and thus the proton transfer process occurs at the time scale of ~1 μs, the conversion from CO_2 to bicarbonate and the subsequent release of bicarbonate must happen at least at an order of magnitude faster than 1 μs. Our current study demonstrates that CAII exhibits negligible structural perturbations (main chain r.m.s.d. less than 0.06 Å) in the amino acid backbones and side chains during CO_2 binding, conversion to bicarbonate, and bicarbonate release (Supplementary Figs. 21 and 22). Therefore, the rapid catalytic reaction of CAII is likely facilitated by the fast dynamics of the active-site water. Previous experimental and computational studies suggest that the dynamics of CAII active-site water molecules exhibit a timescale of picoseconds (ps) to nanoseconds (ns), except for the Zn^{2+}-bound water (W_{Zn}) which shows microseconds (μs) dynamics[64,65]. Thus, the dynamics of active-site waters (W1, W_I, and $W_I{}'$) observed here during the CAII catalysis are predicted to occur on timescales in the ps to ns range.

In this study, we kinetically captured the catalytic intermediates occurring on a sub-ns timescale. This was achieved by combining UV photolysis and temperature-controlled X-ray crystallography. In general, proteins undergo a dynamical transition around 200 K, where their conformational flexibility changes significantly[25]. Below this temperature, they remain in a glassy state, exhibiting minimal conformational flexibility and losing biological function. However, beyond this transition, they regain structural flexibility and biological activity[66]. This transition is closely linked to the dynamical properties of hydration water[67], and in cases where a glass-to-liquid transition of water occurs around proteins, the transition temperature can drop to as low as 110 K[24,68].

In this study, we leveraged the fact that CAII undergoes a dynamical transition around 140 K to capture its catalytic intermediates. When the 3NPA-CAII complex is irradiated with UV light and its temperature is increased from 90 K to 200 K, the thermal energy of the complex increases across all residues (Supplementary Fig. 23). This increment is linear up to ~140 K, indicating increased local atomic vibrations[24]. However, between 140 K and 180 K, the cryogenic water inside the solvent channels of CAII crystals undergoes a glass-to-liquid transition[24,68], leading to a dramatic increase in the flexibility and mobility of the 3NPA-CAII complex (Supplementary Figs. 23 and 24). This increased flexibility and mobility subsequently trigger the catalytic activity of CAII, enabling the kinetic entrapment of its catalytic intermediates at cryogenic temperatures.

Role of active-site water in CAII catalysis

The role of active-site water observed during the CAII catalysis can be summarized as follows (Fig. 7). Initially, a hydroxyl ion is bound to the Zn^{2+} ion, and the three key water molecules (W_{DW}, W1, and W2) are well-organized in the active site (stage (1)). When a CO_2 molecule approaches the active site, it replaces the deep water (W_{DW}) and is stabilized by the hydrophobic interactions within the active site residues (stage (2)). The release of W_{DW} from the active site may partially compensate for the

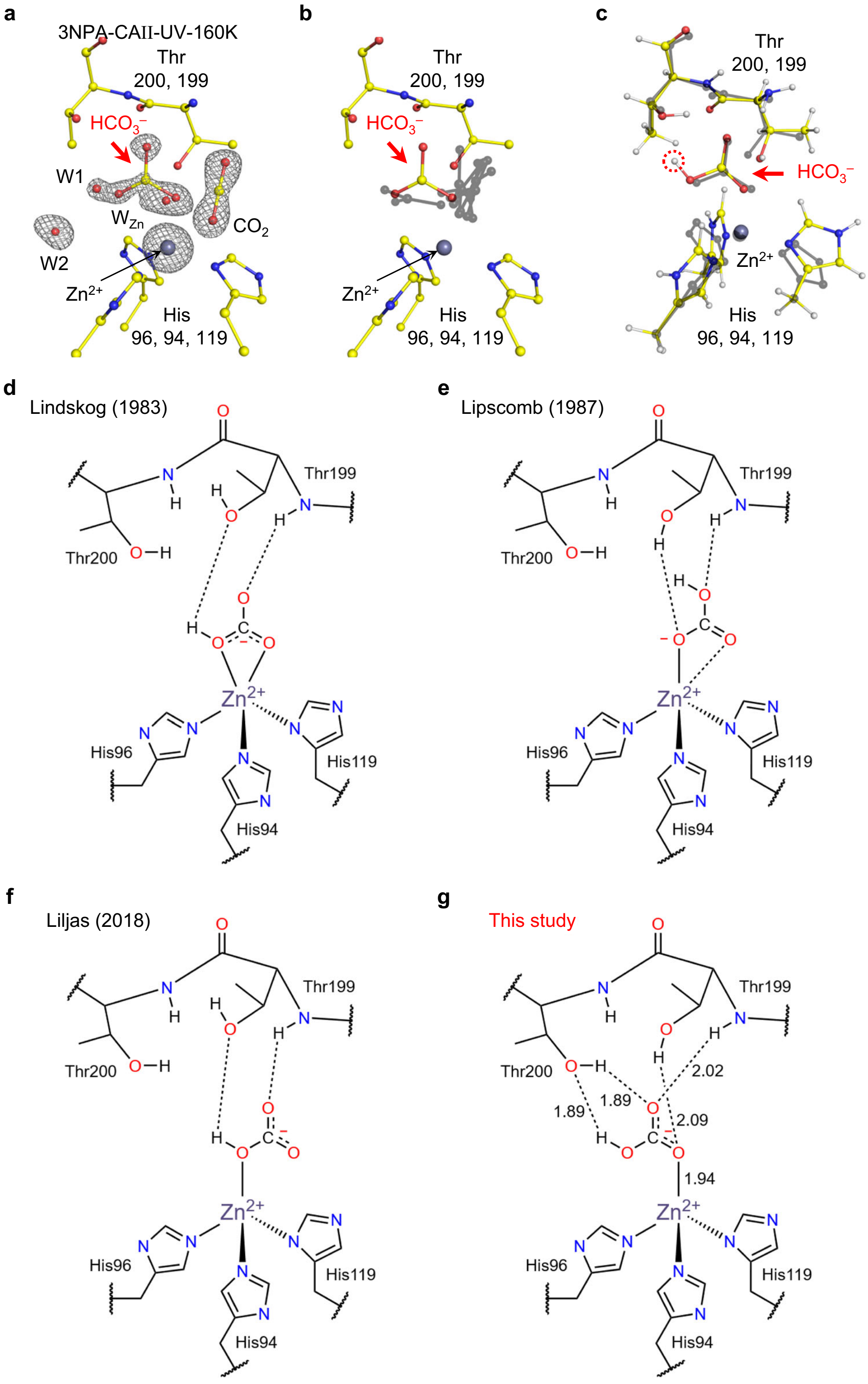

Fig. 5 | Bicarbonate binding configurations in CAII. a In the 3NPA-CAII-UV-160K structure, both CO_2 and bicarbonate were refined. The bicarbonate molecule is located in the electron density map ($2F_o - F_c$ at a cutoff level 1.7σ). The bicarbonate molecule shows steric hindrance with W_{Zn} and W1, resulting in a refinement to 50 % occupancy (Supplementary Fig. 26d). **b** The bicarbonate position observed in this study was compared with six bicarbonate positions previously published: one induced by X-ray radiation in wild-type CAII (PDB ID: 2VVB)[54], two from Co^{2+} and Ni^{2+} substituted CAII (PDB IDs: 6LV2 for the Co^{2+}-CAII; 6LV6 for the Ni^{2+}-CAII)[44,55], and four from CAII mutants (PDB IDs: 1BIC for the T200H CAII variant; 1CAM for the T199A CAII variant; 1LGD for the T199P/C206S CAII variant; 6KM2 for the V143I CAII variant)[56–60]. **c** DFT calculations confirm that the new bicarbonate molecule observed in our study is energetically favorable and identify the location of the hydrogen atom (in a red circle) in the bicarbonate molecule. The gray structure represents the 3NPA-CAII-UV-160K structure used as the starting model for DFT calculation. **d**–**g** Compared with the three previously proposed bicarbonate positions in CAII catalytic mechanisms[29,61,62], the new position in this study is farther from the CO_2 binding site and stabilized by the hydrogen bonding interactions with Thr199 and Thr200.

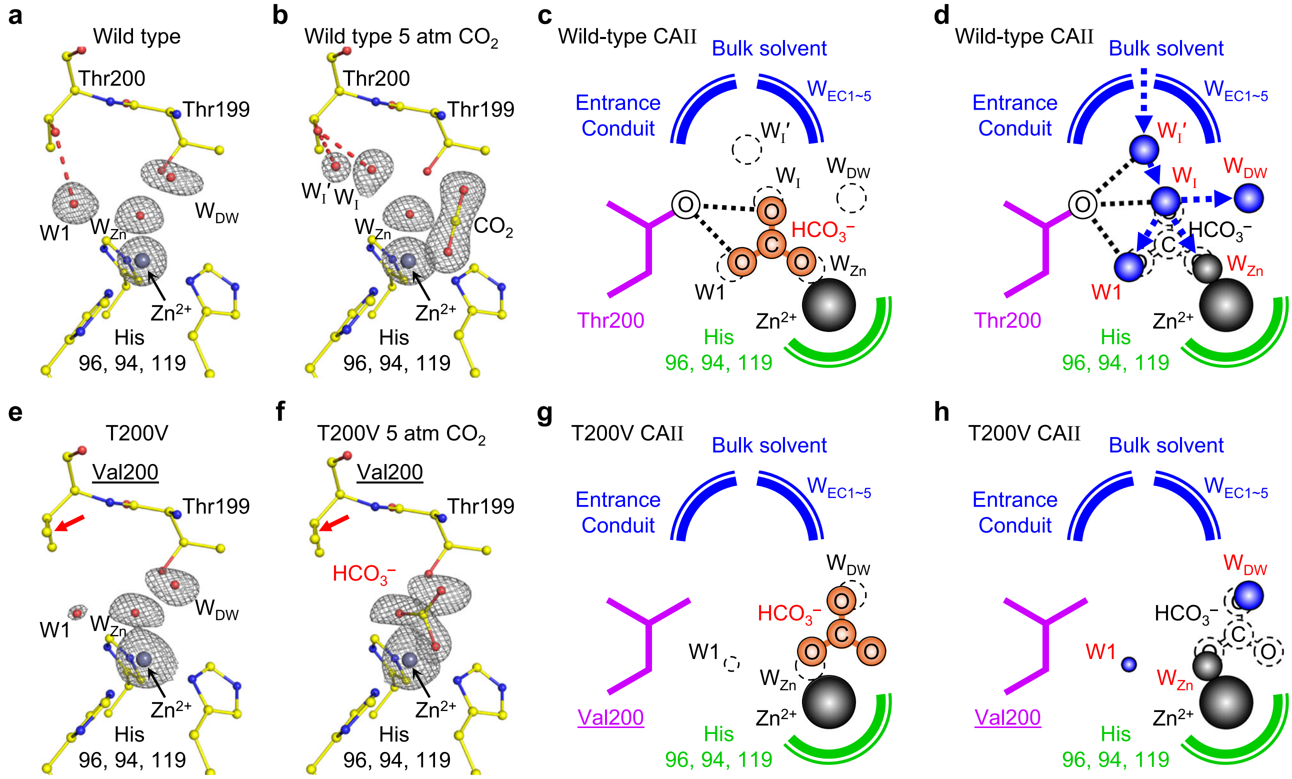

Fig. 6 | The active site of wild-type and T200V CAII upon CO_2 binding. **a** Wild-type CAII shows well-defined waters (W1, W_{Zn}, and W_{DW}) around the Zn^{2+} ion. **b** When the wild-type CAII is exposed to an elevated CO_2 pressure (5 atm), W_{DW} is replaced upon CO_2 binding, and W1 disappears, while two intermediate waters (W_I and W_I´) emerge[44]. Hydrogen bonds between the O atom of Thr200 and three waters (W1, W_I, and W_I´) are represented as red dotted lines. **c** The bicarbonate temporally observed in this study is located near the entrance and overlaps with the stable water molecules (W_{Zn} and W1) and one intermediate water W_I. **d** The bicarbonate molecule competes with incoming water molecules flowing through the intermediate waters (W_I and W_I´) and is eventually released from the active site during the restoration of the active-site water network. **e, f** In the T200V CAII variant (with the T200V mutation marked by a red arrow), W1 water is weakly observed, and neither W_I nor W_I´ are visible when exposed to elevated CO_2 pressure (5 atm). The bicarbonate molecule is more stabilized than the CO_2 molecule. **g** In the T200V CAII, the bicarbonate molecule is captured at a deeper configuration, replacing two water molecules, W_{Zn} and W_{DW}. **h** In the T200V CAII, water inflow appears less efficient due to the absence of intermediate waters (W_I and W_I´), stabilizing the bicarbonate molecule. The electron density maps ($2F_o - F_c$, gray) are contoured at a cutoff level of 1.7σ.

entropy reduction caused by CO_2 binding to the enzyme. Additionally, the stable W1 water shifts to a less stable intermediate position, W_I, upon CO_2 binding. A nucleophilic attack then occurs from the hydroxyl ion to the CO_2 molecule, forming a covalent bond in the transition state (stage (3)). The transition state is negatively charged and significantly stabilized by electrostatic interactions with the Zn^{2+} ion, consistent with the theory of transition state stabilization. When the product (bicarbonate) forms, it pivots rapidly and occupies the positions formerly held by W1 and W_I (Stage (4)). The intermediate W_I water is further displaced to W_I´ by the bicarbonate configuration. The negatively charged bicarbonate molecule is strongly bound to the Zn^{2+} ion. Rapid bicarbonate release is crucial for CAII's turnover and is achieved as outside water molecules flow into the active site through W_I and W_I´, displacing the bicarbonate molecule (stage (5)). After bicarbonate release, a hydroxyl ion forms from the Zn^{2+} bound water, and a proton is transferred out through the ordered water network and His64 (stage (6)), reinitializing the enzyme for the subsequent catalytic cycle.

In conclusion, we have kinetically captured the intermediate states of carbonic anhydrase at the atomic level, uncovering the crucial role of active-site water in its remarkable catalytic efficiency. Given that water is an essential component for all enzymes, our findings suggest that natural enzymes may have evolved to harness the structure and fast dynamics of active-site water in ways beyond our current understanding. An in-depth exploration of the intricate interplay between enzymes and their active-site water is imperative, as it promises to not only profoundly enrich our understanding of molecular evolution but also catalyze breakthroughs in innovative drug design and biocatalyst engineering.

Methods

Protein expression and purification of wild-type and apoCAII

Recombinant CAII was expressed in *Escherichia coli* [BL21 (DE3) pLysS] containing a plasmid encoding the CAII gene[69]. The protein was purified via affinity chromatography[70]. Bacterial cells were enzymatically lysed using hen egg-white lysozyme, and the clarified lysate was applied to an agarose resin functionalized with p-(aminomethyl)-benzene-sulfonamide, a ligand that selectively binds CAII. Bound protein was eluted using 0.4 M sodium azide in 100 mM Tris-HCl at pH 7.0. Sodium azide was subsequently removed through multiple rounds of buffer exchange into 10 mM Tris-HCl pH 8.0.

To generate the zinc-free (apo) form of CAII, the purified wild-type enzyme was incubated at 20 °C for 8 hours in a zinc-chelating buffer composed of 100 mM pyridine 2,6-dicarboxylic acid and 25 mM MOPS, pH 7.0. The resulting solution was then loaded onto a benzylsulfonamide affinity column to separate apoCAII from any remaining holoenzyme. Residual chelating reagent was removed through repeated buffer exchanges using 50 mM Tris-HCl, pH 7.8[36]. The successful removal of zinc ion was confirmed by an esterase activity assay and validated through crystallographic structural analysis. Enzymatic activity was restored upon reconstitution with 1 mM $ZnCl_2$.

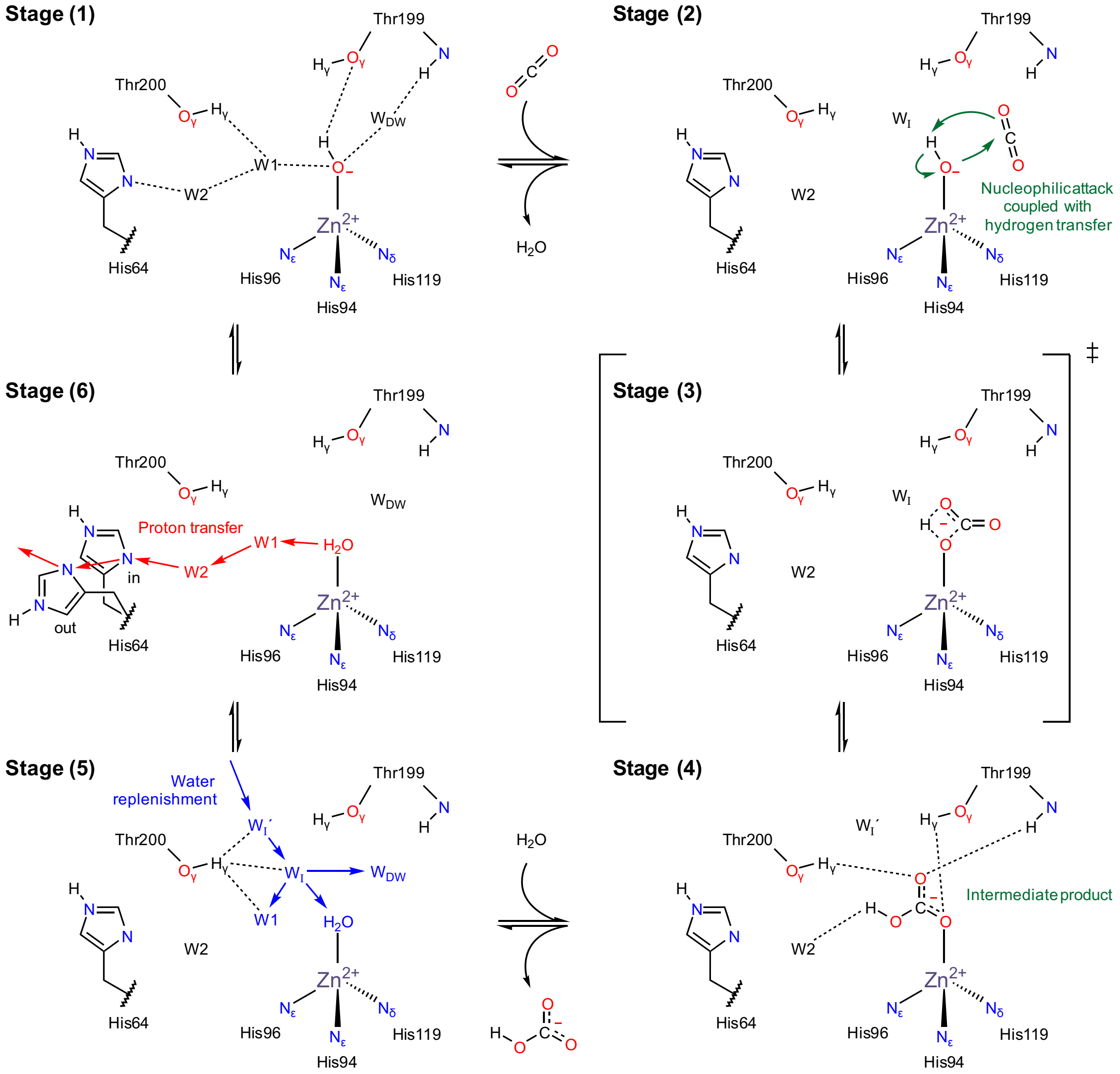

Fig. 7 | Proposed catalytic mechanism of CAII. The Zn^{2+} ion is crucial for generating a hydroxyl ion at physiological pH (stage (1)). Upon CO_2 binding to CAII, the key active-site water molecule W1 shifts to the intermediate position W_I, and a nucleophilic attack occurs (stage (2)). The transition state is stabilized by electrostatic interactions with the Zn^{2+} ion (stage (3)). The product, bicarbonate, then occupies the positions of the three waters (W_{Zn}, W1, and W_I) temporarily (stage (4)) and is eventually replaced with the water molecules flowing through the intermediate positions (W_I and $W_I{}'$) (stage (5)). Finally, a proton is transferred out from the Zn^{2+}-bound water via the proton transfer network (W_{Zn}-W1-W2-His64), restoring the hydroxyl ion (stage (6)). For clarity. the two active-site water molecules (W3a and W3b; Fig. 1b) next to W2 are omitted. Throughout the entire catalytic cycle, the Zn ion does not undergo a redox process and remains in the +2 oxidation state due to its fully filled *d* orbital[91].

Protein expression and purification of T200V CAII variant

To generate the T200V mutation of CAII, a codon at position 200 was optimized for a Threonine to Valine substitution. The mutated plasmid was transformed into *Escherichia coli* [BL21(DE3) pLysS] by heat-shock. Purification was carried out using immobilized metal ion affinity chromatography using His60 Ni-Super flow Resin and FPLC for Size-Exclusion Chromatography using a HiLoad 16/600 Superdex 75 column.

Briefly, bacterial cell lysis was performed by high-pressure homogenizer (EmulsiFlex-C3). After the wash and elute steps, mutant CAII was separated from the resin, and the protein was further fractionated. The solutions that showed absorption at 280 nm UV light were selected and collected. The protein solution was concentrated using an Amicon Ultra-15 Centrifugal Filter Unit (10 kDa) and buffer exchanged using a desalting column. The final concentration of purified mutant CAII solution was 25 mg/ml in 50 mM Tris-HCl, pH 7.8.

Protein crystallization

Crystals of wild-type CAII, apoCAII, and T200V CAII variants were obtained using the hanging drop vapor diffusion method[71]. A 10 µl mixture, consisting of equal volumes of protein (5 µl) and well solution (5 µl), was equilibrated against 500 µl of the well solution (1.3 M sodium citrate, 50 mM Tris-HCl, pH 7.8) at room temperature (~20 °C)[72]. Within a few days, the crystals reached approximate dimensions of ~80 × 160 × 300 μm^3.

Preparation and UV photolysis of 3NPA-CAII, 3NPA-apoCAII, and 3NT-CAII crystals

To prepare 3NPA-CAII and 3NPA-apoCAII complex, single crystals of wild-type and apoCAII were transferred into a soaking solution containing 30 µM 3-Nitrophenyl acetic acid (99%, Sigma-Aldrich), 1.3 M sodium citrate, and 50 mM Tris-HCl at pH 6.8, at room temperature (~20 °C). The crystals were incubated for 30 minutes to allow the 3NPA molecules to infuse into the active site. Once 3NPA soaking was done, the 3NPA-CAII and 3NPA-apoCAII crystals were coated with mineral oil to prevent dehydration and cryocooled under a nitrogen cold stream (90 K) on the synchrotron beamline for X-ray data collection. The 3NT-soaked CAII crystals were prepared using the same soaking procedure, except that the soaking solution was exposed to UV light 12 hours to ensure complete conversion to 3-Nitrotouene prior to soaking.

UV photolysis was employed to trigger the release of CO_2 molecules from 3NPA within the CAII crystal at cryogenic temperatures. While the crystal sample was mounted on the beamline under a nitrogen cold stream (90 K), the sample was illuminated with UV light ($\lambda = 200–400$ nm) from a Xenon fiber optic light source (ASB-XE-175EX, Spectral products). The luminous power emitted by the light source at the sample position was ~100 mW, and the total exposure time was 120 minutes on each of the CAII crystal samples. To ensure that the observed structural changes in 3NPA-CAII were solely due to UV exposure, the experimental setup, especially the translational position of the crystal sample, remained unchanged during UV irradiation process. A photographic overview of the UV irradiation process, along with the UV light source spectrum, is presented in Supplementary Fig. 8. Additionally, images of the crystals used in the experiment are provided in Supplementary Fig. 9.

Cryocooling of wild-type and T200V CAII crystals under CO_2 pressure

Structural determination of wild-type CAII and T200V variant CAII under CO_2 pressure was performed by cryocooling protein crystals under controlled CO_2 pressure[43,44,46,47]. For CO_2 entrapment, a high-pressure cryocooling apparatus designed for X-ray crystallography (HPC-201, Advanced Design Consulting, USA) was utilized. Crystals were coated with mineral oil to prevent dehydration and to serve as a CO_2-absorbing medium, enhancing gas diffusion into the crystals. The oil-coated crystals were then loaded into specialized high-pressure sample tubes[73,74]. Pressurization was conducted at room temperature using CO_2 gas at either atmospheric pressure (0 atm) or elevated pressure (5 atm). After a 5-minute equilibration to allow sufficient gas diffusion, the crystals were cryocooled rapidly in liquid nitrogen (77 K). Once vitrified, the CO_2 gas was released, and the crystals were stored in liquid nitrogen until X-ray diffraction collection.

X-ray diffraction and data collection of 3NPA-CAII and 3NPA-apoCAII crystals

Diffraction data for 3NPA-CAII and 3NPA-apoCAII crystals were collected at the 6D beamline of the Pohang Light Source II (wavelength of 0.9793 Å, beam size of 100 μm) under a nitrogen cold stream (90 K to 200 K). Data were collected using the oscillation method at a 1° step interval and 1 s exposure time on an MX225-HS CCD detector (Rayonix, L.L.C., USA) with a crystal-to-detector distance of 100 mm. A total of 180 images were collected for each of the crystal data sets. During data collection, the sample temperature, ranging from 90 K to 200 K, was controlled by a nitrogen cold stream (Cryojet 5, Oxford Cryosystems), with the temperature being increased at a rate of 5 K/min. After reaching the desired temperature, samples were equilibrated at this temperature for 10 min.

The absorbed X-ray dose for a single data set was less than 3×10^5 Gy. Since seven data sets were collected for each crystal, the total absorbed X-ray dose for the single crystal was less than 2×10^6 Gy, which is below the Henderson dose limit of 1.2×10^7 Gy[75]. Moreover, our earlier studies on CAII verified that X-ray radiation doses of up to 10^7 Gy do not induce noticeable changes in the active site, confirming that the active site structures described in our study are unaffected by X-ray radiation[47]. Indexing, integration, and scaling were performed using HKL2000 (version v716.1)[76]. The data processing statistics are given in Supplementary Tables 2–4.

X-ray diffraction and data collection of 3NPA-CAII crystals at room temperature

Diffraction data for RT-3NPA-CAII crystals were collected at the 5 C beamline of the Pohang Light Source II (wavelength of 0.9794 Å, beam size of 100 μm) at room temperature (~20 °C). Data were collected using the oscillation method at a 1° step interval and 1 s exposure time on the ADSC Quantum 315r CCD detector (Area Detector Systems Corporation, USA) with a crystal-to-detector distance of 150 mm. A total of 30 images were collected from each of the 3NPA-CAII crystals. Data collections were performed at room temperature from 7 fresh crystals coated with mineral oil to prevent dehydration. Single diffraction data set was scaled and merged from the 7 crystal data sets.

The absorbed X-ray dose for each crystal was ~2.1×10^4 Gy, which is smaller than the dose limit of 4.0×10^5 Gy at room temperature[77–80]. Indexing, integration, and scaling were performed using HKL2000 (version v716.1)[76]. The data processing statistics are given in Supplementary Table 5.

X-ray diffraction and data collection of CO_2-3NPA-CAII and CO_2-3NT-CAII crystals

Diffraction data for CO_2-3NPA-CAII and CO_2-3NT-CAII crystals were collected at the 5 C beamline of the Pohang Light Source II (wavelength of 0.8856 Å, beam size of 100 μm) under a nitrogen cold stream at temperature of 100 K. Data were collected using the oscillation method at a 1° step interval and 1 s exposure time on the EIGER X 9 M detector (DECTRIS, Switzerland) with a crystal-to-detector distances of 113.8 mm. A total of 360 images were collected for each of the crystal data sets.

For each data set, a new fresh pressure-cooled crystal was used. The absorbed X-ray dose for a single data set was less than 5×10^5 Gy, which is much smaller than the Henderson dose limit of 1.2×10^7 Gy[75]. Indexing, integration, and scaling were performed using HKL2000 (version v716.1)[76]. The data processing statistics are given in Supplementary Table 6.

X-ray diffraction and data collection of CO_2-wild-type-CAII and CO_2-T200V-CAII crystals

Diffraction data for CO_2-wild-type-CAII and CO_2-T200V-CAII crystals were collected at the 7 A and 6D beamline of the Pohang Light Source II (wavelength of 0.9793 Å, beam size of 100 μm) under a nitrogen cold stream at temperatures of 100 and 90 K, respectively. Data were collected using the oscillation method at a 1° step interval and 1 s exposure time. Two types of CCD detectors were used: the ADSC Quantum 270 (Area Detector Systems Corporation, USA) for the CO_2-wild-type-CAII crystals and MX225-HS CCD detector (Rayonix, L.L.C., USA) for the CO_2-T200V-CAII crystal. The crystal-to-detector distances were set at 120 mm and 100 mm, respectively. A total of 360 images were collected on each of the crystal data sets.

For each data set, a new fresh pressure-cooled crystal was used. The absorbed X-ray dose for a single data set was less than 5×10^5 Gy, which is much smaller than the Henderson dose limit of 1.2×10^7 Gy[75]. Indexing, integration, and scaling were performed using HKL2000 (version v716.1)[76]. The data processing statistics are given in Supplementary Table 7.

Structure determination and model refinement

The CAII structures were determined using the CCP4 program suite (version 6.5.012)[81]. Prior to refinement, a random 5% of the data were flagged for R_{free} analysis. The initial phasing models were based on the previously reported crystal structures[44]: PDB ID of 6LUW for 3NPA-CAII series and CO_2-T200V-CAII, PDB ID of 6LUX for CO_2-wild-type-CAII, and PDB ID of 6LUU for 3NPA-apoCAII series. The maximum likelihood refinement (MLH) was performed using REFMAC5 (version 5.8.0135)[82], followed by manual inspection and adjustment using the molecular graphics program COOT (version 0.9.8.95)[83]. Reiterations of MHL were carried out with an anisotropic B factor. Details on the final refinement statistics are given in Supplementary Tables 2–7.

Upon completing the structural refinements described above, systematic refinements were further carried out to accurately determine the partial occupancies of the CO_2/W_{DW} and $HCO_3^-/(W_{Zn}$ & W1) configurations, described as primary/secondary configurations[44]. A total of 99 structures for each CAII structure were prepared, varying the occupancies between primary and secondary configurations in 1% incremental steps (e.g., the first structure with 1% primary and 99% secondary configuration, the second structure with 2% primary and 98% secondary configuration, ..., the 99th structure with 99% primary and 1% secondary configuration). MLH refinements were carried out in parallel for all 99 structures. Following these refinements, the overall R-factor was plotted as a function of the primary configuration's partial occupancy, and a quadratic function $y = ax^2 + bx + c$ was fitted to the obtained R-factor values, as shown in Supplementary Figs. 25-27. The partial occupancy values of the primary configuration were determined at their minima, $x_{\text{min}} = -b/2a$. To estimate the standard error of this value, we propagated the standard errors of the fitting parameters a and b under the assumption that they are uncorrelated. The error propagated standard error was calculated using the following formula, $\sigma_{x_{\text{min}}} = \sqrt{(b/2a^2)^2\sigma_a^2 + (1/2a)^2\sigma_b^2}$.

Structural analysis of the bound water molecules

To compare the configurations of the bound water molecules in the active site and the entrance conduit, we carefully refined water molecules based on the PDB and COOT validation checks, along with electron density maps ($2F_o - F_c$), using a cutoff level of 1σ[83]. The consistency and reproducibility of the bound water molecules in both the active site and the entrance conduit were rigorously tested. Several water molecules were identified in close proximity within the active site and the entrance conduit of the CAII structures. Recognizing that most of these water molecules are transient and thus could be positioned closer together than stably bound water molecules, we included these closely positioned water molecules in the final coordinates without exclusion. The important ligands and water molecules in the active site are listed in Supplementary Tables 8–13. Additionally, the distance geometry of key residues, ligands, ion, and water molecules is provided in Supplementary Tables 14–20.

Electron density map generation

To visualize the atomic structures of CAII, electron density maps were generated using the FFT function[84]. The $2F_o - F_c$ map was utilized to inspect the overall model refinement and identify discrepancies between the observed data and the model. The $F_o - F_c$ map highlighted regions of difference density, indicating the potential presence of bicarbonate ion. Additionally, $F_{o,B} - F_{o,A}$ maps were generated to analyze the appearance or disappearance of substrate (CO_2) and product (bicarbonate ion) under UV light irradiation or temperature changes. For each figure presented, the contour levels of the electron density maps were adjusted to optimally display the relevant structural features. All structural figures were rendered with PyMOL Molecular Graphics System, (Version 3.1.0a0, Schrödinger, LLC).

Density functional theory calculation

Density functional theory calculations were performed using the Gaussian 16 software[85], and the visualization was achieved using GaussView[86] and VMD[87]. All calculations were performed using the Becke, 3-parameter, Lee–Yang–Parr (B3LYP)[88] hybrid functional with Grimme's dispersion correction (GD3)[89] to account for dispersion interactions, and a large People basis set 6-311 + + G(d,p) was employed. Considering that the active site is deeply buried (15 Å from the protein surface) in a low-dielectric environment, the crystallographic geometry of the active site of CAII was taken for optimization in gas phase. Additionally, the crucial water molecule (W_{Zn}) coordinated to the metal was explicitly included in the calculations. Root-mean-square deviation (r.m.s.d.) values were calculated by aligning the optimized structure with an experimentally determined X-ray structure using VMD. DFT-calculated energies for each catalytic step of wild-type CAII are listed in Supplementary Table 21. Additionally, the distance geometry of bicarbonate-bound CAII structures before and after DFT optimization is provided in Supplementary Table 22.

CO_2 hydration kinetic parameter measurements of CAII with 3NPA and 3NT

The kinetic parameters of CAII for CO_2 hydration in the presence of 3NPA and 3NT were determined using colorimetric stopped-flow spectroscopy with an SX20 stopped-flow system (Applied Photophysics, UK)[90]. All reagent preparations and reactions were conducted at 25 °C. Prior to analysis, the enzyme was dissolved in reaction buffer (100 mM TAPS, 57.2 mM Na_2SO_4, and 97.2 µM m-cresol purple; pH 8.5, adjusted by NaOH), supplemented with a saturated concentration of 3NPA or 3NT, where applicable. The CO_2 hydration reaction was initiated by rapidly mixing equal volumes of the reaction buffer and the CO_2 substrate solution within the stopped-flow cell. Absorbance changes at 578 nm were monitored to track reaction progress. CO_2-saturated deionized water was diluted with N_2-saturated deionized water to prepare substrate solutions with final concentrations ranging from 3.38 mM to 16.9 mM. For each CO_2 concentration, an uncatalyzed CO_2 hydration reaction was performed as a blank experiment. The initial reaction rates, obtained from blank-corrected data, were used to determine the kinetic parameters (k_{cat} and K_M) by fitting the results to the Michaelis-Menten equation.

Reporting summary

Further information on research design is available in the Nature Portfolio Reporting Summary linked to this article.

Data availability

The atomic coordinates and structure factors have been deposited in the Protein Data Bank (http://www.pdb.org/) as [PDB IDs: 7Y2A (3NPA-CAII-noUV-90K), 7Y2C (3NPA-CAII-UV-90K), 7Y2E (3NPA-CAII-UV-120K), 7Y2F (3NPA-CAII-UV-140K), 7Y2G (3NPA-CAII-UV-160K), 7Y2H (3NPA-CAII-UV-180K), and 7Y2I (3NPA-CAII-UV-200K)] for 3NPA-CAII complex, [PDB IDs: 7Y2J (3NPA-apoCAII-noUV-90K), 7Y2K (3NPA-apoCAII-UV-90K), 7Y2L (3NPA-apoCAII-UV-120K), 7Y2M (3NPA-apoCAII-UV-140K), 7Y2N (3NPA-apoCAII-UV-160K), 7Y2O (3NPA-apoCAII-UV-180K), and 7Y2Q (3NPA-apoCAII-UV-200K)] for 3NPA-apoCAII complex, [PDB IDs: 9L2Y (3NPA-CAII-90K), 9L2Z (3NPA-CAII-120K), 9L30 (3NPA-CAII-140K), 9L31 (3NPA-CAII-160K), 9L32 (3NPA-CAII-180K), and 9L33 (3NPA-CAII-200K)] for 3NPA-CAII complex temperature series without UV irradiation, [PDB ID: 9L2X (CO2-3NPA-CAII-15atm)] for 3NPA-CAII cryocooled under CO_2 pressure, [PDB IDs: 9LDO (CO2-3NT-CAII-0atm) and 9LDP (CO2-3NT-CAII-15atm)] for 3NT-CAII cryocooled under CO_2 pressure, [PDB ID: 9LR6 (RT-3NPA-CAII)] for 3NPA-CAII at room temperature, [PDB ID: 8WEP (CO_2-wild-type-CAII-5atm)] for wild-type CAII cryocooled under CO_2 pressure, and [PDB IDs: 8WER (CO_2-T200V-CAII-0atm) and 8WES (CO_2-T200V-CAII-5atm)] for T200V CAII variant cryocooled under CO_2 pressure. Data supporting the findings of the study are available from the corresponding author(s) upon request. Source data are provided with this paper.

References

1. Frey, P. A. & Hegeman, A. D. *Enzymatic reaction mechanisms*. (Oxford University Press, 2007).
2. Wolfenden, R. Benchmark reaction rates, the stability of biological molecules in water, and the evolution of catalytic power in enzymes. *Annu. Rev. Biochem.* **80**, 645–667 (2011).
3. Kraut, J. How do enzymes work? *Science* **242**, 533–540 (1988).

4. Menger, F. M. An alternative view of enzyme catalysis. *Pure Appl. Chem*. **77**, 1873–1886 (2005).
5. Zhang, X. & Houk, K. N. Why enzymes are proficient catalysts: beyond the Pauling paradigm. *Acc. Chem. Res*. **38**, 379–385 (2005).
6. Ringe, D. & Petsko, G. A. Biochemistry. How enzymes work. *Science* **320**, 1428–1429 (2008).
7. Bruice, T. C. & Benkovic, S. J. Chemical basis for enzyme catalysis. *Biochemistry* **39**, 6267–6274 (2000).
8. Cleland, W. W., Frey, P. A. & Gerlt, J. A. The low barrier hydrogen bond in enzymatic catalysis. *J. Biol. Chem*. **273**, 25529–25532 (1998).
9. Gao, J. et al. Mechanisms and free energies of enzymatic reactions. *Chem. Rev*. **106**, 3188–3209 (2006).
10. Koshland, D. Jr Application of a theory of enzyme specificity to protein synthesis. *Proc. Natl Acad. Sci. USA* **44**, 98–104 (1958).
11. Nagel, Z. D. & Klinman, J. P. A 21st century revisionist's view at a turning point in enzymology. *Nat. Chem. Biol*. **5**, 543–550 (2009).
12. Pauling, L. Nature of forces between large molecules of biological interest. *Nature* **161**, 707–709 (1948).
13. Warshel, A. et al. Electrostatic basis for enzyme catalysis. *Chem. Rev*. **106**, 3210–3235 (2006).
14. Schwartz, S. D. & Schramm, V. L. Enzymatic transition states and dynamic motion in barrier crossing. *Nat. Chem. Biol*. **5**, 551–558 (2009).
15. Nashine, V. C., Hammes-Schiffer, S. & Benkovic, S. J. Coupled motions in enzyme catalysis. *Curr. Opin. Chem. Biol*. **14**, 644–651 (2010).
16. Cheatum, C. M. Low-Frequency Protein Motions Coupled to Catalytic Sites. *Annu. Rev. Phys. Chem*. **71**, 267–288 (2020).
17. Benkovic, S. J. & Hammes-Schiffer, S. A perspective on enzyme catalysis. *Science* **301**, 1196–1202 (2003).
18. Bhabha, G. et al. A dynamic knockout reveals that conformational fluctuations influence the chemical step of enzyme catalysis. *Science* **332**, 234–238 (2011).
19. Hay, S. & Scrutton, N. S. Good vibrations in enzyme-catalysed reactions. *Nat. Chem*. **4**, 161–168 (2012).
20. Henzler-Wildman, K. & Kern, D. Dynamic personalities of proteins. *Nature* **450**, 964–972 (2007).
21. Kamerlin, S. C. & Warshel, A. At the dawn of the 21st century: Is dynamics the missing link for understanding enzyme catalysis? *Proteins* **78**, 1339–1375 (2010).
22. Kohen, A. Role of dynamics in enzyme catalysis: substantial versus semantic controversies. *Acc. Chem. Res*. **48**, 466–473 (2015).
23. Ma, B. & Nussinov, R. Enzyme dynamics point to stepwise conformational selection in catalysis. *Curr. Opin. Chem. Biol*. **14**, 652–659 (2010).
24. Kim, C. U., Tate, M. W. & Gruner, S. M. Protein dynamical transition at 110 K. *Proc. Natl Acad. Sci. USA* **108**, 20897–20901 (2011).
25. Ringe, D. & Petsko, G. A. The 'glass transition' in protein dynamics: what it is, why it occurs, and how to exploit it. *Biophys. Chem*. **105**, 667–680 (2003).
26. Frauenfelder, H. et al. A unified model of protein dynamics. *Proc. Natl Acad. Sci. USA* **106**, 5129–5134 (2009).
27. Levy, Y. & Onuchic, J. N. Water mediation in protein folding and molecular recognition. *Annu. Rev. Biophys*. **35**, 389–415 (2006).
28. Grossman, M. et al. Correlated structural kinetics and retarded solvent dynamics at the metalloprotease active site. *Nat. Struct. Mol. Biol*. **18**, 1102–1108 (2011).
29. Spiro, T. G. Zinc enzymes. (J. Wiley New York, 1983).
30. Davenport, H. W. The early days of research on carbonic anhydrase. *Ann. N. Y. Acad. Sci*. **429**, 4–9 (1984).
31. Chegwidden, W. R., Carter, N. D. & Edwards, Y. H. *The carbonic anhydrases: new horizons*. Vol. 90 (Birkhäuser, 2013).
32. Frost, S. C. & McKenna, R. *Carbonic anhydrase: mechanism, regulation, links to disease, and industrial applications*. Vol. 75 (Springer Science & Business Media, 2013).
33. Supuran, C. T. & De Simone, G. *Carbonic anhydrases as biocatalysts: from theory to medical and industrial applications*. (Elsevier, 2015).
34. Meldrum, N. U. & Roughton, F. J. Carbonic anhydrase. Its preparation and properties. *J. Physiol*. **80**, 113–142 (1933).
35. Liang, J. Y. & Lipscomb, W. N. Theoretical-Study of Carbonic Anhydrase-Catalyzed Hydration of CO2 - a Brief Review. *Int. J. Quantum Chem*. **36**, 299–312 (1989).
36. Håkansson, K., Carlsson, M., Svensson, L. A. & Liljas, A. Structure of native and apo carbonic anhydrase II and structure of some of its anion-ligand complexes. *J. Mol. Biol*. **227**, 1192–1204 (1992).
37. Lindskog, S. & Silverman, D. N. The catalytic mechanism of mammalian carbonic anhydrases. In *The Carbonic Anhydrases* 175–195 (2000).
38. Silverman, D. N. & McKenna, R. Solvent-mediated proton transfer in catalysis by carbonic anhydrase. *Acc. Chem. Res*. **40**, 669–675 (2007).
39. Krishnamurthy, V. M. et al. Carbonic anhydrase as a model for biophysical and physical-organic studies of proteins and protein-ligand binding. *Chem. Rev*. **108**, 946–1051 (2008).
40. Liljas, A. et al. Crystal structure of human carbonic anhydrase C. *Nat. N. Biol*. **235**, 131–137 (1972).
41. Eriksson, A. E., Jones, T. A. & Liljas, A. Refined structure of human carbonic anhydrase II at 2.0 Å resolution. *Proteins* **4**, 274–282 (1988).
42. Christianson, D. W. & Fierke, C. A. Carbonic anhydrase: Evolution of the zinc binding site by nature and by design. *Acc. Chem. Res*. **29**, 331–339 (1996).
43. Kim, J. K. et al. Active-site solvent replenishment observed during human carbonic anhydrase II catalysis. *IUCrJ* **5**, 93–102 (2018).
44. Kim, J. K. et al. Elucidating the role of metal ions in carbonic anhydrase catalysis. *Nat. Commun*. **11**, 4557 (2020).
45. Silverman, D. N. & Lindskog, S. The Catalytic Mechanism of Carbonic-Anhydrase - Implications of a Rate-Limiting Protolysis of Water. *Acc. Chem. Res*. **21**, 30–36 (1988).
46. Domsic, J. F. et al. Entrapment of carbon dioxide in the active site of carbonic anhydrase II. *J. Biol. Chem*. **283**, 30766–30771 (2008).
47. Kim, C. U. et al. Tracking solvent and protein movement during CO2 release in carbonic anhydrase II crystals. *Proc. Natl Acad. Sci. USA* **113**, 5257–5262 (2016).
48. Margerum, J. D. & Petrusis, C. T. Photodecarboxylation of nitrophenylacetate ions. *J. Am. Chem. Soc*. **91**, 2467–2472 (1969).
49. Lommel, K. et al. Caged CO2 for the direct observation of CO2-consuming reactions. *ChemBioChem* **14**, 372–380 (2013).
50. Hirakawa, Y. et al. Characterization of a novel type of carbonic anhydrase that acts without metal cofactors. *BMC Biol*. **19**, 105 (2021).
51. Yadav, S., Kalita, S. & Dubey, K. D. Mechanism of a novel metal-free carbonic anhydrase. *Phys. Chem. Chem. Phys*. **26**, 28124–28132 (2024).
52. Lindskog, S. & Malmström, B. G. Metal binding and catalytic activity in bovine carbonic anhydrase. *J. Biol. Chem*. **237**, 1129–1137 (1962).
53. Lindskog, S. & Nyman, P. O. Metal-Binding Properties of Human Erythrocyte Carbonic Anhydrases. *Biochim Biophys. Acta* **85**, 462–474 (1964).
54. Sjoblom, B., Polentarutti, M. & Djinovic-Carugo, K. Structural study of X-ray induced activation of carbonic anhydrase. *Proc. Natl Acad. Sci. USA* **106**, 10609–10613 (2009).
55. Hakansson, K. & Wehnert, A. Structure of cobalt carbonic anhydrase complexed with bicarbonate. *J. Mol. Biol*. **228**, 1212–1218 (1992).
56. Xue, Y. et al. Crystallographic analysis of Thr-200 -> His human carbonic anhydrase II and its complex with the substrate, HCO3-. *Proteins* **15**, 80–87 (1993).

57. Xue, Y., Liljas, A., Jonsson, B. H. & Lindskog, S. Structural analysis of the zinc hydroxide-Thr-199-Glu-106 hydrogen-bond network in human carbonic anhydrase II. *Proteins* **17**, 93–106 (1993).
58. Huang, S., Sjoblom, B., Sauer-Eriksson, A. E. & Jonsson, B. H. Organization of an efficient carbonic anhydrase: implications for the mechanism based on structure-function studies of a T199P/C206S mutant. *Biochemistry* **41**, 7628–7635 (2002).
59. West, D. et al. Structural and kinetic effects on changes in the CO2 binding pocket of human carbonic anhydrase II. *Biochemistry* **51**, 9156–9163 (2012).
60. Kim, J. K. et al. Structural insights into the effect of active-site mutation on the catalytic mechanism of carbonic anhydrase. *IUCrJ* **7**, 985–994 (2020).
61. Liang, J. Y. & Lipscomb, W. N. Hydration of carbon dioxide by carbonic anhydrase: Internal protein transfer of Zinc (2+)-bound bicarbonate. *Biochemistry* **26**, 5293–5301 (1987).
62. Liljas, A. Carbonic anhydrase under pressure. *IUCrJ* **5**, 4–5 (2018).
63. Behravan, G., Jonsson, B. H. & Lindskog, S. Fine tuning of the catalytic properties of human carbonic anhydrase II. *Eff. varying Act.-site residue 200. Eur. J. Biochem.* **195**, 393–396 (1991).
64. Denisov, V. P., Jonsson, B.-H. & Halle, B. Dynamics of Functional Water in the Active Site of Native Carbonic Anhydrase from 17O Magnetic Relaxation Dispersion. *J. Am. Chem. Soc.* **121**, 2327–2328 (1999).
65. Singh, H. et al. Fast microsecond dynamics of the protein-water network in the active site of human carbonic anhydrase ii studied by solid-state NMR spectroscopy. *J. Am. Chem. Soc.* **141**, 19276–19288 (2019).
66. Rasmussen, B. F., Stock, A. M., Ringe, D. & Petsko, G. A. Crystalline ribonuclease A loses function below the dynamic transition at 220 K. *Nature* **357**, 423–424 (1992).
67. Fenimore, P. W., Frauenfelder, H., McMahon, B. H. & Parak, F. G. Slaving: Solvent fluctuations dominate protein dynamics and functions. *Proc. Natl Acad. Sci. USA* **99**, 16047–16051 (2002).
68. Kim, C. U., Tate, M. W. & Gruner, S. M. Glass-to-cryogenic-liquid transitions in aqueous solutions suggested by crack healing. *Proc. Natl Acad. Sci. USA* **112**, 11765–11770 (2015).
69. Forsman, C., Behravan, G., Osterman, A. & Jonsson, B.-H. Production of active human carbonic anhydrase ll in E. coli. *Acta Chem. Scand.* **42**, 314–318 (1988).
70. Khalifah, R. G., Strader, D. J., Bryant, S. H. & Gibson, S. M. Carbon-13 nuclear magnetic resonance probe of active-site ionizations in human carbonic anhydrase B. *Biochemistry* **16**, 2241–2247 (1977).
71. McPherson, A. *Preparation and analysis of protein crystals*. (John Wiley & Sons, 1982).
72. Fisher, S. Z. et al. Atomic crystal and molecular dynamics simulation structures of human carbonic anhydrase II: Insights into the proton transfer mechanism. *Biochemistry* **46**, 2930–2937 (2007).
73. Kim, C. U., Kapfer, R. & Gruner, S. M. High-pressure cooling of protein crystals without cryoprotectants. *Acta Crystallogr. D.* **61**, 881–890 (2005).
74. Kim, C. U., Hao, Q. & Gruner, S. M. Solution of protein crystallographic structures by high-pressure cryocooling and noble-gas phasing. *Acta Crystallogr. D.* **62**, 687–694 (2006).
75. Henderson, R. Cryo-protection of protein crystals against radiation damage in electron and X-ray diffraction. *Proc. R. Soc. B* **241**, 6–8 (1990).
76. Otwinowski, Z. & Minor, W. [20] Processing of X-ray diffraction data collected in oscillation mode. *Methods Enzymol.* **276**, 307–326 (1997).
77. Barker, A. I., Southworth-Davies, R. J., Paithankar, K. S., Carmichael, I. & Garman, E. F. Room-temperature scavengers for macromolecular crystallography: increased lifetimes and modified dose dependence of the intensity decay. *J. Synchrotron Rad.* **16**, 205–216 (2009).
78. Warkentin, M. et al. Global radiation damage at 300 and 260 K with dose rates approaching 1 MGy s−1. *Acta Crystallogr. D.* **68**, 124–133 (2012).
79. Fischer, M. Macromolecular room temperature crystallography. *Q. Rev. Biophys.* **54**, e1 (2021).
80. de la Mora, E. et al. Radiation damage and dose limits in serial synchrotron crystallography at cryo-and room temperatures. *Proc. Natl Acad. Sci. USA* **117**, 4142–4151 (2020).
81. Bailey, S. The Ccp4 Suite - programs for protein crystallography. *Acta Crystallogr. D.* **50**, 760–763 (1994).
82. Murshudov, G. N., Vagin, A. A. & Dodson, E. J. Refinement of macromolecular structures by the maximum-likelihood method. *Acta Crystallogr. D.* **53**, 240–255 (1997).
83. Emsley, P. & Cowtan, K. Coot: model-building tools for molecular graphics. *Acta Crystallogr. D.* **60**, 2126–2132 (2004).
84. Ten Eyck, L. F. Crystallographic fast Fourier transforms. *Acta Crystallogr. A* **29**, 183–191 (1973).
85. Frisch, M. J. et al. Gaussian 16 Revision C.01 (Wallingford, CT, 2016).
86. Dennington, R., Keith, T. & Millam, J. GaussView, version 5. (2009).
87. Humphrey, W., Dalke, A. & Schulten, K. VMD: visual molecular dynamics. *J. Mol. Graph.* **14**, 33–38 (1996).
88. Lee, C. T., Yang, W. T. & Parr, R. G. Development of the colle-salvetti correlation-energy formula into a functional of the electron-density. *Phys. Rev. B* **37**, 785–789 (1988).
89. Grimme, S., Antony, J., Ehrlich, S. & Krieg, H. A consistent and accurate ab initio parametrization of density functional dispersion correction (DFT-D) for the 94 elements H-Pu. *J. Chem. Phys.* **132**, 154104 (2010).
90. Khalifah, R. G. The carbon dioxide hydration activity of carbonic anhydrase: I. Stop-flow kinetic studies on the native human isoenzymes B and C. *J. Biol. Chem.* **246**, 2561–2573 (1971).
91. Williams, R. J. P. The biochemistry of zinc. *Polyhedron* **6**, 61–69 (1987).

Acknowledgements

The authors would like to thank the staff at Pohang Light Source II for their support in data collection. Experiments at PLS-II beamlines (6D, 7 A, and 11 C) were supported in part by MSIT, POSTECH, and UNIST Central Research Facilities. Use of the Stanford Synchrotron Radiation Lightsource was supported by the U.S. Department of Energy (No. DE-AC02-76SF00515), and the SSRL Structural Molecular Biology Program was supported by the DOE Office and by the National Institutes of Health (P30GM133894). Use of resources at the Center for High-Energy X-ray Sciences (CHEXS) was supported by the National Science Foundation (DMR-2342336), and the Macromolecular Diffraction at CHESS (MacCHESS) facility was supported by the National Institute of General Medical Sciences and the National Institutes of Health (award 1-P30-GM124166). This work was supported by the Samsung Science and Technology Foundation (SSTF-BA1702-04 to C.U.K.) and the National Research Foundation of Korea (RS-2022-NR070463 & RS-2022-00154676 to C.U.K.; RS-2024-00353098 to C.-M.G.; 2021R1C1C1010943 to J.-M.C.; 2020R1C1C1003937 to D.M.; 2021R1A5A8029490 to B.H.J.).

Author contributions

J.K.K. and C.U.K. conceived the research, J.K.K., C.Lee, J.T.A., C.Lomelino and T.J.S. ran the experiment on the wild-type and apoCAII, S.W.L., H.J., S.K. and D.M. ran the experiment on the T200V CAII variant, D.W.S. and B.H.J. measured the CA kinetics, R.K. and J.-M.C. carried out the DFT calculations, J.K.K. and C.U.K. analysed the data and wrote the manuscript. J.L.W., A.E.C., C.-M.G. and R.M. contributed to the overall scientific interpretation and edited the manuscript.

Competing interests

The authors declare no competing interests.

Additional information

Supplementary information The online version contains supplementary material available at https://doi.org/10.1038/s41467-025-59645-x.

Correspondence and requests for materials should be addressed to Chae Un Kim.

Peer review information *Nature Communications* thanks Gloria Borgstahl, Kshatresh Dubey, and the other anonymous reviewer(s) for their contribution to the peer review of this work. A peer review file is available.

Reprints and permissions information is available at http://www.nature.com/reprints